

# Turbulence in Primordial Dark Matter Halos and Its Impact on the First Star Formation

MENG-YUAN HO,<sup>1,2</sup> KE-JUNG CHEN,<sup>1,3</sup> AND PEI-CHENG TUNG<sup>1,2</sup>

<sup>1</sup>*Institute of Astronomy and Astrophysics, Academia Sinica, Taipei 10617, Taiwan*

<sup>2</sup>*Department of Physics, National Taiwan University, Taipei 10617, Taiwan*

<sup>3</sup>*Heidelberg Institute for Theoretical Studies, Schloss-Wolfsbrunnenweg 35, Heidelberg 69118, Germany*

## ABSTRACT

We present high-resolution simulations of the first star-forming clouds in 15 minihalos with masses ranging from  $\sim 10^5$  to  $10^7 M_\odot$  at redshifts  $z \sim 17$ – $20$ , using the GIZMO code. Our simulations incorporate detailed primordial gas physics and adopt initial conditions from the state-of-the-art IllustrisTNG cosmological simulations. To achieve the required resolution, we apply a particle-splitting technique that increases the resolution of the original IllustrisTNG data by a factor of  $\sim 10^5$ , reaching gas and dark matter particle masses of  $0.2 M_\odot$  and  $80 M_\odot$ , respectively. This enables us to resolve gas accretion during the early assembly of minihalos and to capture the emergence of strong turbulent flows. We find that turbulence, driven by gas infall into the dark matter potential wells, is predominantly supersonic, with characteristic Mach numbers ranging from 1.8 to 4.2, increasing with halo mass. The supersonic turbulence effectively fragments the central gas cloud into multiple dense clumps, some of which form gravitationally bound cores and begin to collapse into the first stars. Our results suggest that supersonic turbulence is a common feature in minihalos and plays a key role in generating clumpy star-forming clouds, with important implications for the initial mass function of the first stars.

**Keywords:** Cosmology — Population III Stars — Turbulence — Star Formation — Metal-Poor Stars — Supersonic Turbulence

## 1. INTRODUCTION

The first generation of stars, known as Population III (Pop III) stars, formed from pristine primordial gas composed primarily of hydrogen and helium. These stars are believed to have formed in dark matter halos with masses of  $10^5$ – $10^6 M_\odot$  (Tegmark et al. 1997; Bromm et al. 2002; Norman 2008). In the absence of metals, the only efficient coolant in these early clouds at temperatures below  $10^4$  K is molecular hydrogen, which enables gas to cool down to  $\sim 200$  K and initiates gravitational collapse (Yoshida et al. 2003; Stiavelli 2009). Unlike present-day star formation, the lack of metal-line cooling in primordial environments results in significantly higher Jeans masses, leading to the formation of more massive stars (Abel et al. 2002; Yoshida et al. 2003). Early theoretical studies suggest that Pop III stars formed with masses ranging from 40 to  $500 M_\odot$ , far exceeding the typical stellar masses observed in the local universe (Tegmark et al. 1997; Abel et al. 1998; Omukai 2001; Omukai & Palla 2003; O’Shea & Norman 2007; Hirano et al. 2014; Hosokawa et al. 2016; Klessen & Glover 2023). However, observations of extremely metal-poor (EMP) stars—believed to be second-generation stars enriched by Pop III supernovae—indicate that their progenitors may have had lower masses, in the range of  $25$ – $50 M_\odot$  (Umeda & Nomoto 2005; Ishigaki et al. 2018; Skúladóttir et al. 2024; Ji et al. 2024). The formation of Pop III stars is influenced by several physical processes, including turbulence, radiative feedback, and magnetic fields (Menon et al. 2020a,b; Mathew & Federrath 2021; Grudić et al. 2022; He & Ricotti 2023; Sharda & Menon 2024). We propose that the apparent discrepancy between theoretical predictions and observational constraints may stem from the limited resolution in previous simulations, which often failed to capture the emergence and effects of turbulence during minihalo assembly (Turk et al. 2009; Stacy et al. 2010; Hirano et al. 2014; Greif 2015; Chen et al. 2015). These previous studies used hierarchical zoom-in techniques to resolve the central star-forming regions with high-resolution of sub-pc scale, but the larger-scale environment of the halo of  $100$ – $1000$  pc remained poorly resolved, making it challenging to model the emergence of turbulence from gas accretion during halo assembly.

The recent study by Chen et al. (2025) was the first to demonstrate the presence of supersonic turbulence emerging during the formation of minihalos. Their simulations revealed that this turbulence can drive fragmentation at the cloud scale, potentially influencing both the subsequent star formation and the characteristic mass scale of Pop III stars. However, Chen et al. (2025) focused on a single, massive minihalo of  $\sim 10^7 M_\odot$ , leaving the general nature and prevalence of turbulence in minihalos largely

unexplored. In this study, we extend [Chen et al. \(2025\)](#) to a broader sample of halos to investigate the diversity of turbulence in the early universe. We select a suite of minihalos from the large-scale cosmological simulation *IllustrisTNG*, and enhance the resolution by a factor of  $10^5$  through a particle-splitting technique. This enables us to resolve the gas accretion onto halos and capture the development of turbulence within primordial gas clouds. This paper is to characterize the physical properties of turbulent gas, examine its dependence on host halo properties, and assess its role in shaping the initial conditions for Pop III star formation.

The structure of this paper is as follows. In Section 2, we describe the *GIZMO* code, including the method used to initialize conditions from the *IllustrisTNG* simulations and the implementation of the particle-splitting algorithm. In Section 3, we present the formation of supersonic turbulence in minihalos and examine the physical properties of clumpy star-forming regions. Section 4 discusses the astrophysical implications of our findings, and we conclude in Section 5.

## 2. METHODS

In this section, we describe the details of our simulation setup. The initial conditions are derived from the *IllustrisTNG* project, a state-of-the-art large-scale cosmological simulation that captures the hierarchical growth of structure and the evolution of baryons and dark matter across cosmic time. From the *IllustrisTNG* snapshot at  $z \approx 20$ , we identify and select 15 minihalos with masses in the range of  $10^5$ – $10^7 M_\odot$ , representing the typical environments for the Pop III star formation. These halos are then extracted from *IllustrisTNG* and re-simulated using the *GIZMO* code in meshless finite mass (MFM) mode, which allows for accurate modeling of gas dynamics in complex astrophysical environments.

Since the simulation resolution of the *IllustrisTNG* is insufficient to resolve the small-scale gas dynamics within these minihalos, we employ a particle-splitting algorithm to increase the resolution by a factor of  $10^5$ . This procedure significantly refines the mass resolution of gas particles, enabling us to resolve the turbulent gas accretion and fragmentation processes that occur during the assembly of minihalo.

### 2.1. *GIZMO*

*GIZMO*, developed by [Hopkins \(2015\)](#), is a robust hydrodynamics code based on the Meshless Finite Mass (MFM) and Meshless Finite Volume (MFV) methods. It evolves from the widely used *GADGET-2* code ([Springel 2005](#)), originally designed for N-body/SPH cosmological simulations. Like *GADGET-2*, *GIZMO* employs a Tree Particle-Mesh (TreePM) algorithm ([Xu 1995](#); [Bagla 2002](#); [Bode & Ostriker 2003](#); [Hopkins 2015](#)) for gravitational calculations, enabling accurate and efficient force evaluations by hierarchically decomposing the simulation volume.

The MFM/MFV approach in *GIZMO* replaces the traditional smoothed-particle hydrodynamics (SPH) kernel summation with a volume-discretized formulation that combines the strengths of both SPH and grid-based Eulerian methods. This hybrid formulation allows for superior accuracy in capturing shocks, contact discontinuities, and turbulent flows while maintaining excellent conservation properties and numerical stability. *GIZMO* has been rigorously validated in a wide range of astrophysical and cosmological test problems, establishing its reliability for high-resolution simulations.

#### 2.1.1. *Physics of Primordial Gas*

We model the cooling and chemistry of primordial gas in our *GIZMO* simulations using *GRACKLE* ([Smith et al. 2017](#)), a publicly available chemistry and cooling library. *GRACKLE* tracks a non-equilibrium network of twelve primordial species:  $\text{H}$ ,  $\text{H}^+$ ,  $\text{H}^-$ ,  $\text{D}$ ,  $\text{D}^+$ ,  $\text{HD}$ ,  $\text{H}_2$ ,  $\text{H}_2^+$ ,  $\text{He}$ ,  $\text{He}^+$ ,  $\text{He}^{++}$ ,  $\text{e}^-$ . The associated gas cooling processes include collisional excitation and ionization, radiative recombination, free-free emission, and other atomic cooling mechanisms for hydrogen and helium. Additionally, *GRACKLE* accounts for molecular cooling from  $\text{H}_2$  and  $\text{HD}$  through rotational and vibrational line emission, formation heating/cooling, and collision-induced emission. The chemistry and cooling network is self-consistently coupled with the hydrodynamic evolution, allowing for accurate modeling of the thermal and chemical state of primordial gas.

#### 2.2. *Mini-Halos in the IllustrisTNG*

The *IllustrisTNG* project is a state-of-the-art suite of large-scale cosmological magnetohydrodynamical simulations designed to study galaxy formation and evolution from redshift  $z = 127$  to  $z = 0$  ([Nelson et al. 2018](#); [Naiman et al. 2018](#); [Springel et al. 2018](#); [Marinacci et al. 2018](#)). These simulations are performed using the moving-mesh code *AREPO* ([Springel 2010](#); [Weinberger et al. 2016](#); [Pillepich et al. 2018](#)) and cover a wide range of cosmic volumes, mass resolutions, and baryonic physics. For this study, we utilize the highest-resolution dataset from the TNG50-1 run, which is particularly suitable for modeling minihalos. The baryonic mass resolution in TNG50-1 is approximately  $8.5 \times 10^4 M_\odot$ , and the dark matter mass resolution is about  $4.5 \times 10^5 M_\odot$ .

We identify minihalo candidates using the SUBFIND algorithm (Springel et al. 2001) through the publicly available IllustrisTNG data release<sup>1</sup>. Our selection criteria are as follows: we search for halos with total masses of  $10^5 - 10^7 M_\odot$  in the earliest snapshot at  $z = 20.05$ . We further restrict our selection to halos that are non-star-forming and relatively isolated, excluding those that undergo major mergers between  $z \approx 20$  and  $z \approx 15$ . Based on these criteria, we select 15 minihalo candidates of total masses in the range  $4.9 \times 10^5$  to  $7.7 \times 10^6 M_\odot$ . For each halo, we extract a comoving spherical volume of radius  $\sim 10$  ckpc from IllustrisTNG that encompasses the halo and its surrounding medium. This volume is then mapped directly onto our GIZMO simulations as the zoom-in initial conditions.

### 2.3. Cosmological Zoom-in Simulations via particle-splitting

These TNG halos originally contained only tens to hundreds of gas and dark matter particles. Such a mass resolution is too low to resolve the structure of the gas flow. To further increase the mass resolution of the initial conditions of TNG50-1, we apply the super-Lagrangian refinement introduced in Hopkins (2015), an algorithm for splitting particles to increase the mass resolution of the original TNG50-1 halos. This method is widely used in zoom-in simulations, e.g. Tung & Chen (2024); Ramesh & Nelson (2024); Ramesh et al. (2024).

To resolve the turbulence produced in the simulation, we need to increase the mass resolution of approximately  $8.38 \times 10^4 M_\odot \rightarrow 0.19 M_\odot$  for gas particles and  $4.56 \times 10^5 M_\odot \rightarrow 80.88 M_\odot$  for dark-matter particles. The particle splitting algorithm operates as the following steps:

1. **Criterion Check for Splitting** Determine if a particle meets the splitting criteria. Specifically, a particle is eligible for splitting if its mass exceeds two times the targeted masses, which are  $0.19 M_\odot$  for gas and  $80.88 M_\odot$  for dark matter.
2. **Determining Spacing of child particles** Before splitting a particle, determine the spacing of the new particles. The code searches for the nearest particle to the target particle and then calculates the effective radius on the basis of the distance between them or the softening length. The spacing distance is set to the minimum of the two values: 0.70 of the effective radius, which is determined by the radius to enclose 32 neighbors; Or 0.25 of the softening length with a cubic spline kernel.
3. **Splitting** If the particle satisfies the splitting criteria, it will be divided into two new particles, each with a half mass of the original particle. The positions of the two particles are randomly adjusted within a specified direction and separated by the spacing distance while maintaining the conservation of mass, momentum, and inertial momentum.

Using this particle-splitting algorithm, we can achieve the desired mass resolution to resolve the turbulent gas during the formation of minihalos. Particle splitting is applied during the first five million years of the simulation. In this phase, only the self-gravity of gas and dark matter, along with gas hydrodynamics, is active. The splitting proceeds gradually, progressively refining particle masses and enabling the resolution of evolving structures driven by gravitational collapse. By 5 Myr, the particle masses reach the target resolution for both gas and dark matter, and dense gas structures begin to emerge. Unlike adaptive mesh refinement (AMR) methods, which refine only preselected regions of interest, our particle-splitting approach is applied uniformly to all particles within the simulation domain. This strategy ensures consistent mass resolution throughout the entire volume, providing a more complete picture of the developing turbulence.

After reaching the desired resolution, we activate the primordial gas cooling and non-equilibrium chemistry modules using the GRACKLE library, and continue to evolve the mini-halo. Since our objective is to investigate the formation of turbulence during the gravitational assembly of minihalos without stellar feedback, we intentionally exclude any prescriptions for star formation. Toward the end of the simulations, the dense gas undergoes rapid collapse due to Jeans instability, which drastically reduces the simulation timestep because of the Courant–Friedrichs–Lewy (CFL) condition (Gnedin et al. 2018). This computational slowdown ultimately leads to the termination of the simulation. As a result, each model evolves over a slightly different duration, typically from  $z = 20$  to  $z = 18.96$ – $18.26$ , corresponding to 14.17–24.80 million years of physical time. For consistency, we use the final available snapshot from each model for our analysis.

### 2.4. Clump-Finding Algorithm

Similar to present-day star formation, strong turbulence can typically produce clumpy structures of dense gas that host star formation. To quantify the clumpy structures in our simulations, we identify gas clumps within the central regions of the minihalos

<sup>1</sup> <https://www.tng-project.org/data/>

using the clump finder module in the YT analysis toolkit (Turk et al. 2011), a Python-based platform for volumetric data visualization and analysis. The clump-finding algorithm, originally developed by Smith et al. (2009) and Turk et al. (2009), operates by iteratively tracing isodensity contours starting from a selected high-density region, referred to as the master clump. A clump is defined as a region enclosed by the lowest isodensity surface that contains a local density maximum, following the method described by Truelove et al. (1998). However, only the gravitationally bound clumps are considered viable sites for Pop III star formation.

### 3. PRIMORDIAL GAS IN MINI HALOS

Our simulations include a sample of 15 minihalos, each exhibiting distinct evolutionary behaviors. The detailed properties of each minihalo at the time of analysis are summarized in Table 1.

Halo	Virial Radius [pc]	Virial Mass [ $10^5 M_\odot$ ]	Gas [ $10^5 M_\odot$ ]	Dark Matter [ $10^5 M_\odot$ ]	Time [Myr]
<b>A</b>	121.79	4.90	0.62	4.28	17.41
<b>B</b>	133.74	6.37	0.87	5.49	17.71
<b>C</b>	162.23	11.10	1.38	9.73	19.97
<b>D</b>	161.42	11.54	1.16	10.38	18.61
<b>E</b>	180.83	14.01	1.43	12.58	24.80
<b>F</b>	196.59	18.90	1.75	17.15	22.13
<b>G</b>	202.43	22.54	2.18	20.36	17.11
<b>H</b>	213.30	25.43	2.74	22.68	18.91
<b>I</b>	219.86	28.51	2.81	25.69	14.17
<b>J</b>	235.86	32.72	2.25	30.46	21.20
<b>K</b>	245.31	37.20	4.80	32.40	19.21
<b>L</b>	252.61	45.87	4.25	41.62	14.17
<b>M</b>	282.98	56.85	4.13	52.72	20.28
<b>N</b>	277.38	59.22	4.94	54.27	14.46
<b>O</b>	311.67	77.08	6.61	70.47	21.51

**Table 1.** Physical properties of minihalos at the end of the simulations.

#### 3.1. Physical properties of primordial star-forming cloud

During the formation of minihalos, the gravitational potential well formed by dark matter traps the surrounding primordial gas and concentrates it in the halo centers. Due to the tidal force from dark matter and inhomogeneous accretion, the accreting gas flow becomes highly anisotropic. Multiple accretion streams are injected into the center of the halo and drive a turbulent gas cloud. We select three models including **Halo A** ( $4.90 \times 10^5 M_\odot$ ), **Halo H** ( $2.54 \times 10^6 M_\odot$ ), and **Halo N** ( $7.71 \times 10^6 M_\odot$ ) to present small, medium and large halo masses for comparison. We first show the density slice of these models at the end of the simulations in Figure 1. The gas distribution inside the halos looks highly complicated with the filamentary structure. The high-dense region is located by the halo centers, which are likely to become the nursing site of Pop III stars. In Figure 2, we show the corresponding temperature distribution. The high-dense regions normally correspond to the low-temperature regions. The average temperature of the halos is  $\sim 1000\text{--}2000$  K, and the center is of a few hundred K that are caused by molecular hydrogen cooling. The high-density region can form molecular hydrogen more efficiently and cool to a lower temperature.

The phase diagrams of **Halo A**, **H**, and **N** are shown in Figure 3. A prominent feature in all three models is the broad distribution of gas particles spanning from the low-density, high-temperature regime to the high-density, low-temperature regime. This trend reflects the primordial gas cooling processes included in our models. Initially, the simulations begin with diffuse and warm gas. As the halos evolve, gas accretes toward the central regions of the minihalos. With increasing density, molecular hydrogen ( $\text{H}_2$ ) cooling becomes increasingly efficient, resulting in a gradual temperature decline at high densities. This cooling continues until the gas reaches the temperature floor set by  $\text{H}_2$  and HD cooling, typically around  $100\text{--}200$  K, depending on the local gas density (Glover & Abel 2008).

#### 3.2. Supersonic turbulence of primordial gas



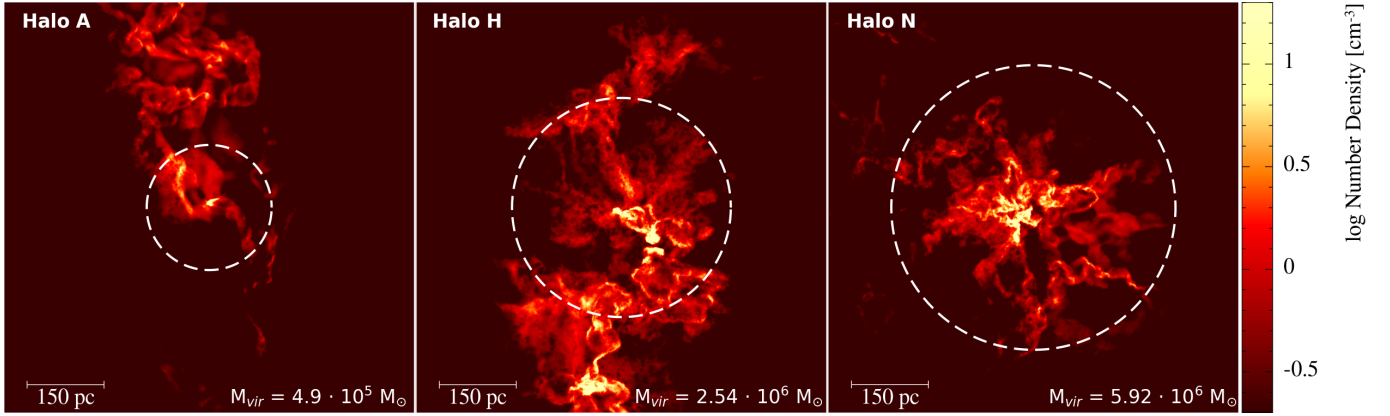


**Figure 1.** Gas density of **A**, **H**, and **N** halos at the end of the simulations. The bright color represents the high-dense region. The white dashed circles show the virial sphere of the halo which increase with the halo mass. Fragmental structure appears at the halo centers, implying the turbulence formation due to gas accretion.

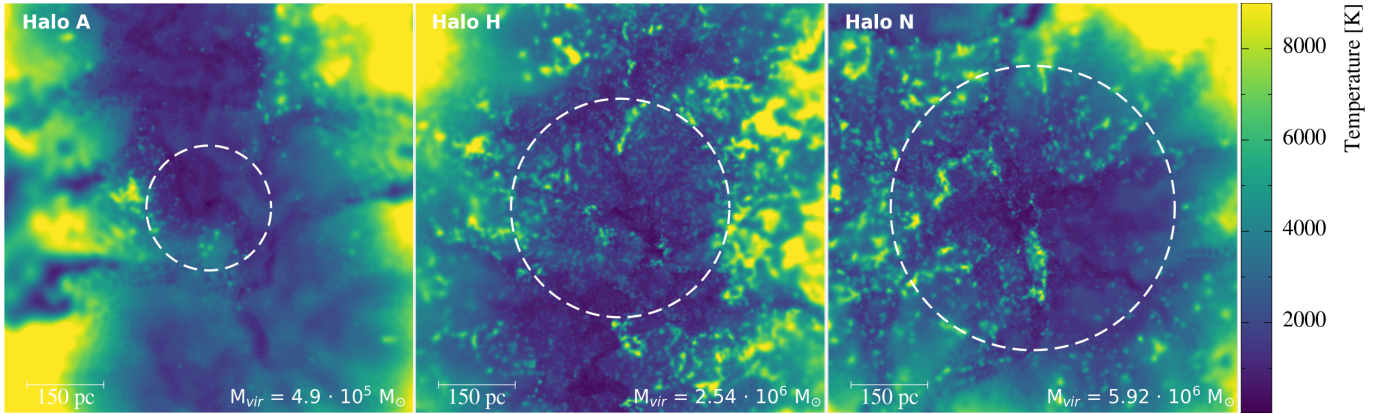


**Figure 2.** Gas temperatures of **A**, **H**, and **N** halos at the end of the simulations. The white dashed circles indicates the virial sphere of the halo. Most of the cool gas accumulated at the halo centers to due to the effective molecular hydrogen cooling. The cool gas can cool to a temperature of several hundred K, corresponding to the high-dense region shown in Figure 1.

We examine the gas kinematics in the minihalos by presenting the gas density distribution and velocity streamlines in Figure 4. The streamlines originate from large-scale gas accretion beyond the halo virial radius and exhibit complex, twisted patterns that converge toward the halo centers. This morphology indicates the presence of strong turbulent and convergent flows within the halos.

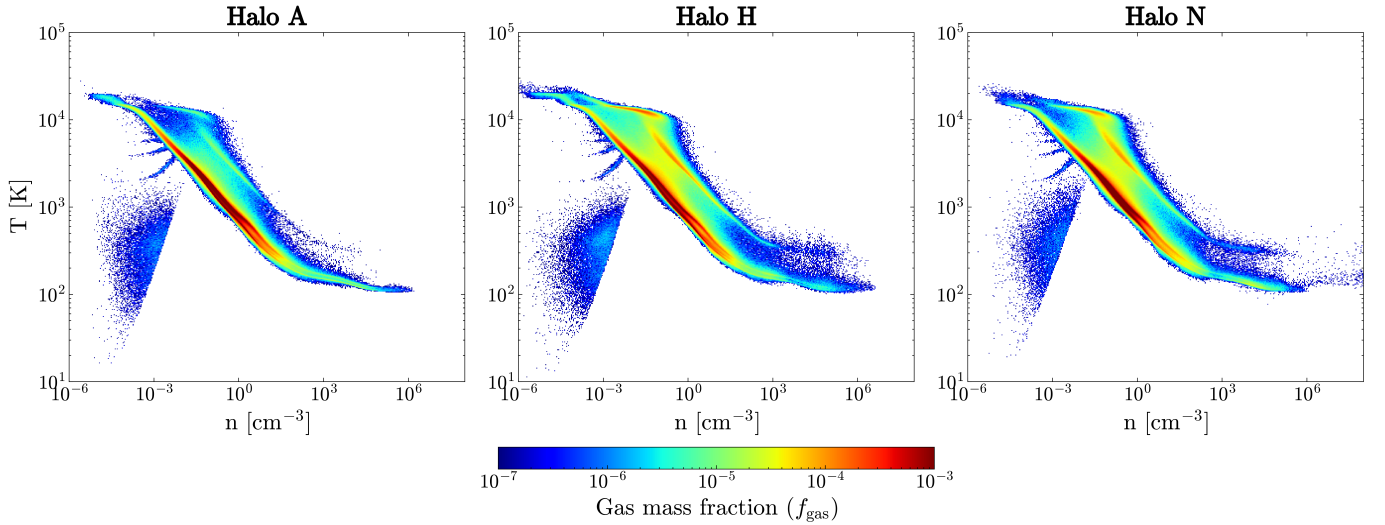
### 3.3. Kinetic Energy power spectrum

To quantify the flow kinematics within the halo, we show the gas kinetic energy power spectra of models **A**, **H**, and **N** in Figure 5. The normalized spectra exhibit a power-law decay with a slope broadly consistent with the Kolmogorov spectrum (Kolmogorov 1991; Shukurov 2011). The classical Kolmogorov spectrum can be divided into three characteristic regimes—from large to small scales: the energy injection (driving) scale, the inertial range, and the dissipation scale.

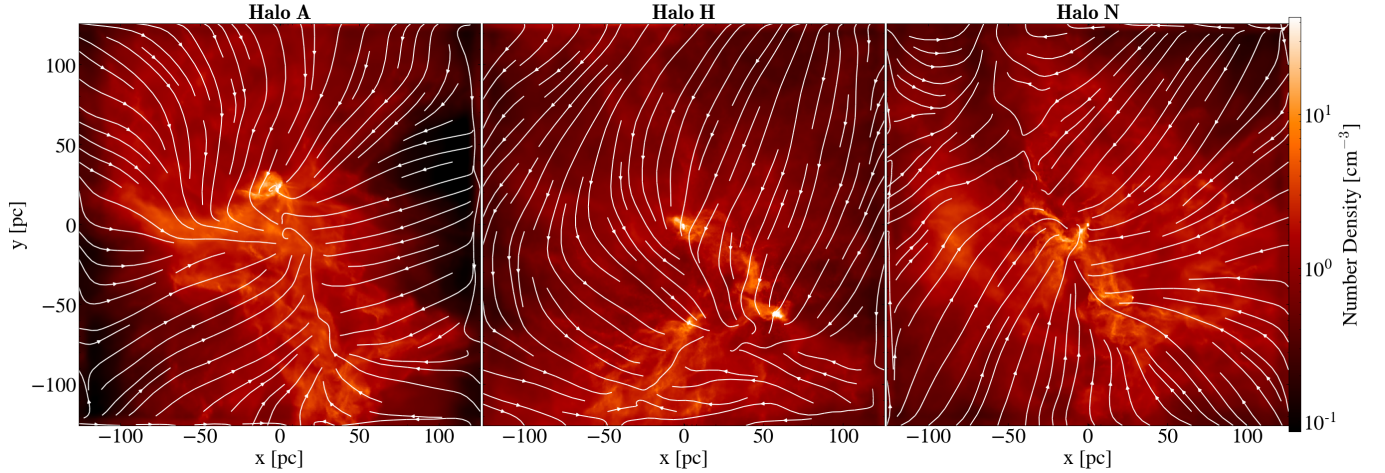
In Figure 5, we identify a turning point at a small wavenumber  $k \sim 1 \text{ kpc}^{-1}$ , corresponding to a physical scale of approximately 800–1,000 pc. This scale separates the energy-driving regime from the inertial range. Given that the typical virial radius of our minihalos is  $R_{200} \approx 100\text{--}300 \text{ pc}$  (see Table 1), this suggests that the largest turbulent eddies have scales of  $\sim 3\text{--}5 R_{\text{vir}}$ .

At scales smaller than the driving scale, the power spectra follow the expected Kolmogorov slope of  $k^{-5/3}$ , consistent with the inertial range where turbulent energy cascades without loss. The eventual dissipation of turbulence occurs at atomic scales (Yuen et al. 2022), which are not resolved in our simulations. Instead, turbulence is dissipated through numerical viscosity at the particle-mesh level.

### 3.4. Supersonic Turbulence



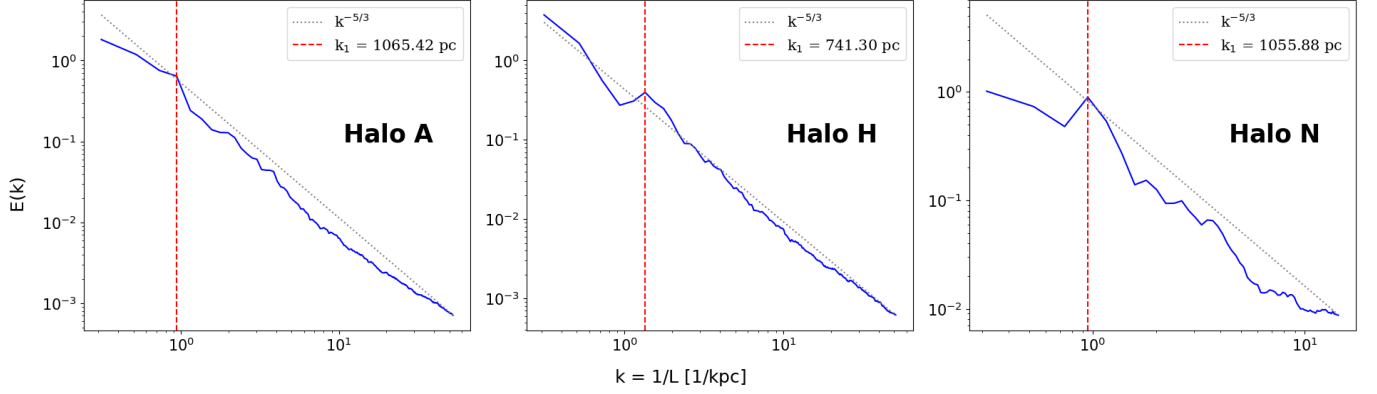
**Figure 3.** Gas temperature–density phase diagram at the end of the simulations. The gas spans a density range from  $10^{-5}$  to  $10^6 \text{ cm}^{-3}$ , with corresponding temperatures from  $\sim 10$  to  $10^4 \text{ K}$ . In the low-density regime ( $10^{-5} < n < 10^{-2} \text{ cm}^{-3}$ ), the gas temperature increases with density due to adiabatic compression. At higher densities ( $n > 10^{-2} \text{ cm}^{-3}$ ), efficient radiative cooling by molecular hydrogen ( $\text{H}_2$ ) and deuterated hydrogen ( $\text{HD}$ ) causes the temperature to decrease as density increases. A distinct component of warm gas with  $T \sim 10^4 \text{ K}$  is also present, originating from shock-heated, low-density gas in the outer regions of the halos.



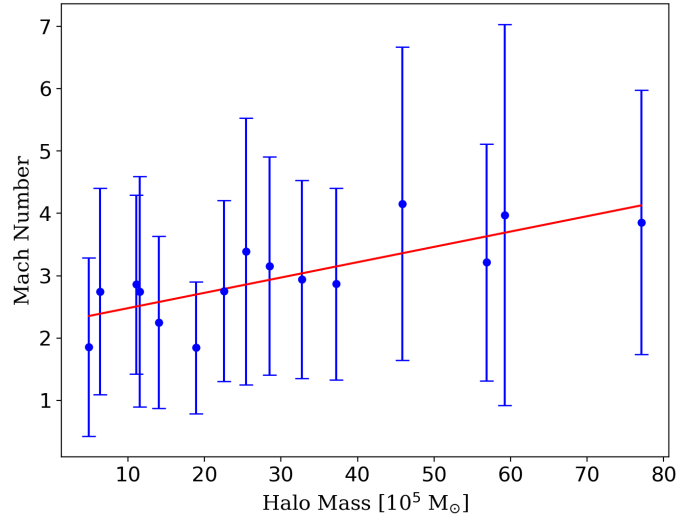
**Figure 4.** Gas accretion onto minihalos. Stream lines represent the flow pattern of accreting gas. These lines converge to dense clumps at the halo center and stir up the turbulence gas.

We now examine the characteristic turbulent Mach number ( $\mathcal{M}$ ) in our simulations. The  $\mathcal{M}$  quantifies the ratio of gas velocity to the local sound speed and is defined as  $\mathcal{M} \equiv v/c_s$ , where  $v$  is the gas velocity relative to the bulk motion, and  $c_s$  is the local sound speed. We focus our analysis on the gas within each halo and present the relationship between  $\mathcal{M}$  and halo mass in Figure 6. Our results reveal a positive correlation between the characteristic  $\mathcal{M}$  and the halo’s virial mass. Specifically,  $\mathcal{M}$  increases with increasing halo mass, with typical values ranging from  $\mathcal{M} \approx 1.9$  to  $4.1$  for halos with masses between  $4.9 \times 10^5 M_\odot$  and  $7.7 \times 10^6 M_\odot$ . The error bars indicate a scatter of  $\mathcal{M} = 1-3$ , depending on the specific halo. This trend suggests that more massive minihalos generate stronger turbulent flows, likely due to deeper gravitational potentials and higher infall velocities.

Furthermore, we show the gas mass fraction as a function of the  $\mathcal{M}$  in Figure 7. While the overall distribution appears similar across different halos, we note that the maximum  $\mathcal{M}$  in model N reaches up to  $\sim 35$ , whereas most other models exhibit peak  $\mathcal{M}$  values below 25. The characteristic  $\mathcal{M}$  number — corresponding to the peak of the curves in Figure 7 — lies within the range of 3–5 for all models. Interestingly, the high- $\mathcal{M}$  tail extends further for more massive halos. About 0.01–0.1% of the gas can reach  $\mathcal{M} \geq 10$ . Given a total halo gas mass of  $\sim 10^6 M_\odot$ , this implies that roughly  $1000 M_\odot$  of gas can reach such high  $\mathcal{M}$  numbers.



**Figure 5.** Kinetic energy spectra of halo gas for **Halo A, H, and N**. The x-axis shows the wave number in units of  $[\text{kpc}^{-1}]$ , and the y-axis indicates the normalized kinetic energy of the gas. The red dashed lines mark the change of spectra slope. The black dashed lines represent the Kolmogorov spectrum following  $k^{-5/3}$ , which closely matches the computed spectra from the halo gas, confirming the presence of turbulence in the halo environment.



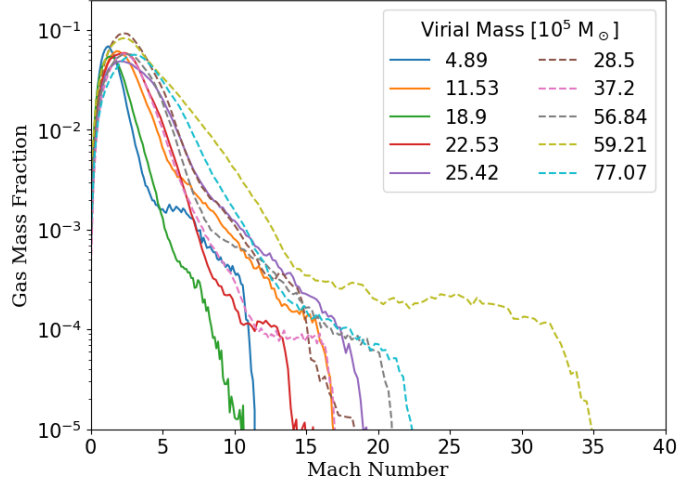
**Figure 6.** The relation between the mean  $\mathcal{M}$  and its halo mass. The mean  $\mathcal{M}$  ranges from 1.8 to 3.8, roughly increasing with the halo mass. The red line shows the best fit profile for the data points, which the average  $\mathcal{M}$  increases by one as the halo mass increases by  $2.8 \times 10^6 M_\odot$ .

Figure 8 shows the gas mass fraction as a function of number density. We find a consistent trend across all models: the peak mass fraction is located at  $n \approx 1 \text{ cm}^{-3}$ , corresponding to the inner halo region. A vertical line marks  $n = 10^5 \text{ cm}^{-3}$ , the typical density threshold for the primordial gas to collapse into Pop III stars (Omukai & Palla 2001; Bromm et al. 2002; Chen et al. 2015). All models exhibit varying fractions of gas exceeding this threshold, indicating that star-forming conditions are achieved to different extents across the halos.

### 3.5. Clumpy structures of the first-star clouds

We use a clump-finding approach to identify the number, morphology, and mass of star-forming clouds. Figure 9 shows the final snapshot of the clump distributions based on this method. Multiple gas clumps are found in each halo, and at this stage, one gravitationally bound clump has formed in every halo. These bound clumps are undergoing Jeans instability and are expected to collapse imminently to form stars.

The mass of each clump provides an upper limit for the mass of the Pop III star that may form within it. Therefore, both the mass and number of clumps set important constraints on the characteristic mass scale and initial mass function (IMF) of Pop III stars. We summarize the physical properties of these clumps in Table 2. Across all halos, clump masses range from  $2.6 M_\odot$  to  $66.5 M_\odot$ , with central densities from  $4.8 \times 10^5$  to  $3.81 \times 10^9 \text{ cm}^{-3}$ , and temperatures between 111–321 K. All clumps exceed their corresponding Jeans masses, confirming their gravitational instability.



**Figure 7.** Gas mass fraction as a function of  $\mathcal{M}$ . The distribution follows an approximately log-normal shape for  $\mathcal{M} < 10$ , with an extended high- $\mathcal{M}$  tail reaching values of  $\mathcal{M} \sim 10\text{--}35$ . As the halo mass increases, both the peak of the distribution and the extent of the high- $\mathcal{M}$  tail shift toward higher  $\mathcal{M}$ , indicating stronger turbulence in more massive minihalos.

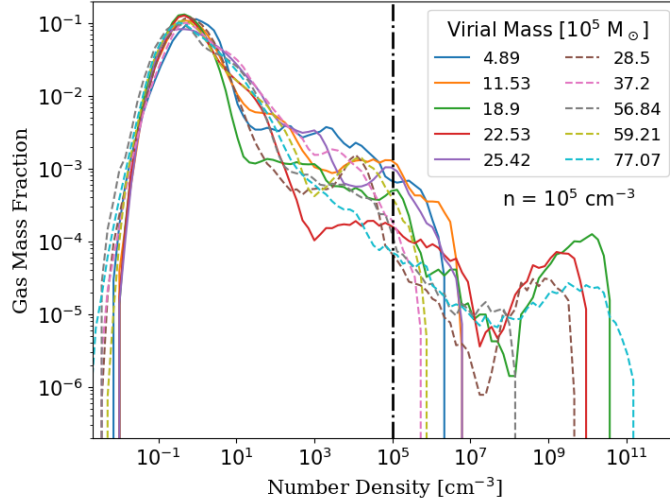


**Figure 8.** Gas mass fraction as a function of its number density. A vertical dot-dashed line marks  $n = 10^5 \text{ cm}^{-3}$ , commonly considered the critical density for the gravitational collapse of the first star-forming gas. For densities below  $n \lesssim 10^2 \text{ cm}^{-3}$ , the mass fraction profiles are remarkably similar across all halos. However, at higher densities ( $n > 10^2 \text{ cm}^{-3}$ ), the profiles begin to diverge significantly, reflecting varying degrees of dense gas formation and collapse in different minihalos.

Once a clump begins to collapse, the simulation timestep rapidly decreases—by a factor of  $\sim 10^4$ —which effectively halts the simulation. To follow the collapse further, higher resolution or the introduction of sink particles is necessary. Some unbound clumps visible in Figure 9 may eventually become gravitationally bound if the simulations are allowed to proceed longer.

#### 4. DISCUSSION

Previous studies were unable to resolve and follow the formation of primordial turbulence during the early assembly of minihalos. [Abel et al. \(1998\)](#); [Bromm \(2013\)](#) suggested that turbulence within the first star-forming clumps is subsonic and plays a limited role in star formation. However, these earlier works typically employed hierarchy zoom-in techniques using AMR or SPH, with the highest-resolution only for a small regions at center of the minihalos. As a result, they lacked sufficient resolution on larger scales to capture the full development of accretion flows and turbulence found in [Chen et al. \(2025\)](#).

Our simulations successfully resolve the formation and evolution of turbulence during minihalo assembly. This turbulence is driven primarily by gravitational potential energy released during gas accretion onto the minihalos. We find that most of the halo



Halo	$r_{\text{eff}}$ [pc]	$M_{\text{clump}}$ [ $M_{\odot}$ ]	$M_J$ [ $M_{\odot}$ ]	$n$ [ $\text{cm}^{-3}$ ]	$T_c$ [K]
A	0.049	13.79	2.99	$1.14 \times 10^6$	111.44
B	0.024	12.58	0.29	$2.30 \times 10^9$	294.57
C	0.050	11.96	3.50	$7.62 \times 10^5$	108.35
D	0.066	55.97	3.02	$2.23 \times 10^6$	140.46
E	0.035	50.21	0.62	$7.56 \times 10^7$	158.22
F	0.024	28.85	0.23	$3.44 \times 10^9$	294.68
G	0.031	66.50	0.52	$8.98 \times 10^8$	321.84
H	0.019	2.62	2.37	$2.90 \times 10^6$	130.31
I	0.024	8.12	0.41	$4.81 \times 10^8$	222.83
J	0.024	8.48	0.24	$3.81 \times 10^9$	308.16
K	0.059	7.89	5.72	$3.13 \times 10^5$	111.67
L	0.047	12.35	3.16	$1.11 \times 10^6$	114.71
M	0.019	10.36	0.87	$2.03 \times 10^7$	128.33
N	0.028	61.96	0.81	$1.47 \times 10^8$	235.78
O	0.063	13.31	5.06	$4.48 \times 10^5$	116.04

**Table 2.** Physical properties of the star-forming clump in each halo. The table lists clump size ( $r_{\text{eff}}$ ), mass ( $M_{\text{clump}}$ ), jeans mass ( $M_J$ ), and peak density ( $\rho_{\text{max}}$ ).  $r_{\text{eff}}$  is defined by  $(3V_c/4\pi)^{1/3}$ , where  $V_c$  is the volume of the clump.  $M_J$  here is estimated according to Equation 2 in [Chen et al. \(2024\)](#). These clumps exceeding their jeans should collapse and form into stars shortly.

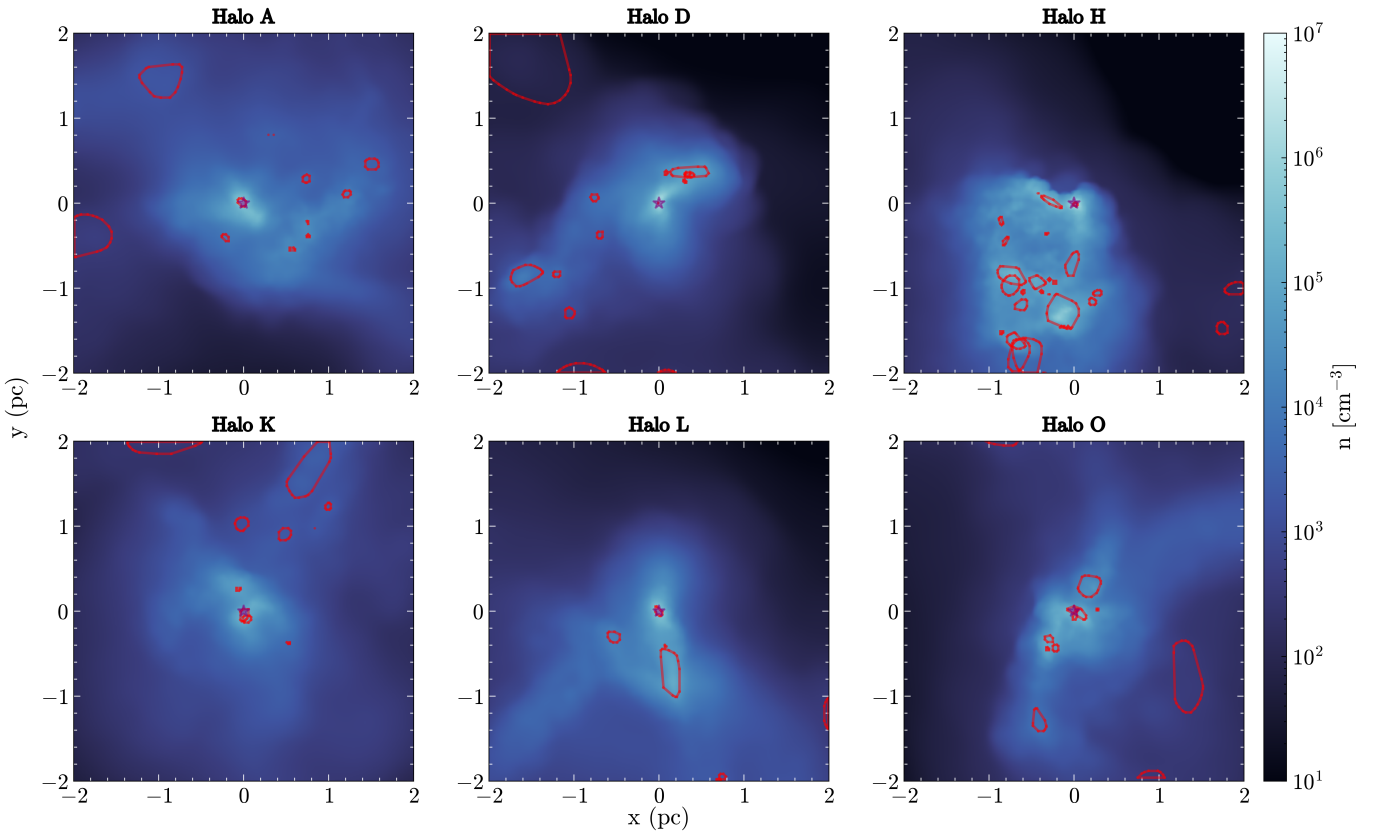


**Figure 9.** Clumpy structures within the central regions of the minihalos. Red contours trace gas clumps that emerge from turbulent flows. While many of these clumps are not yet gravitationally bound, they may become bound over time through continued gas accretion. At the current stage of the simulation, only the densest clump marked with red stars—located at the halo center—has reached the threshold for gravitational binding, and its core has begun to collapse due to Jeans instability.

gas become supersonic with a characteristic  $\mathcal{M}$  of  $\sim 2$ – $5$ , consistent with those adopted in driven turbulence simulations by [Tang](#)



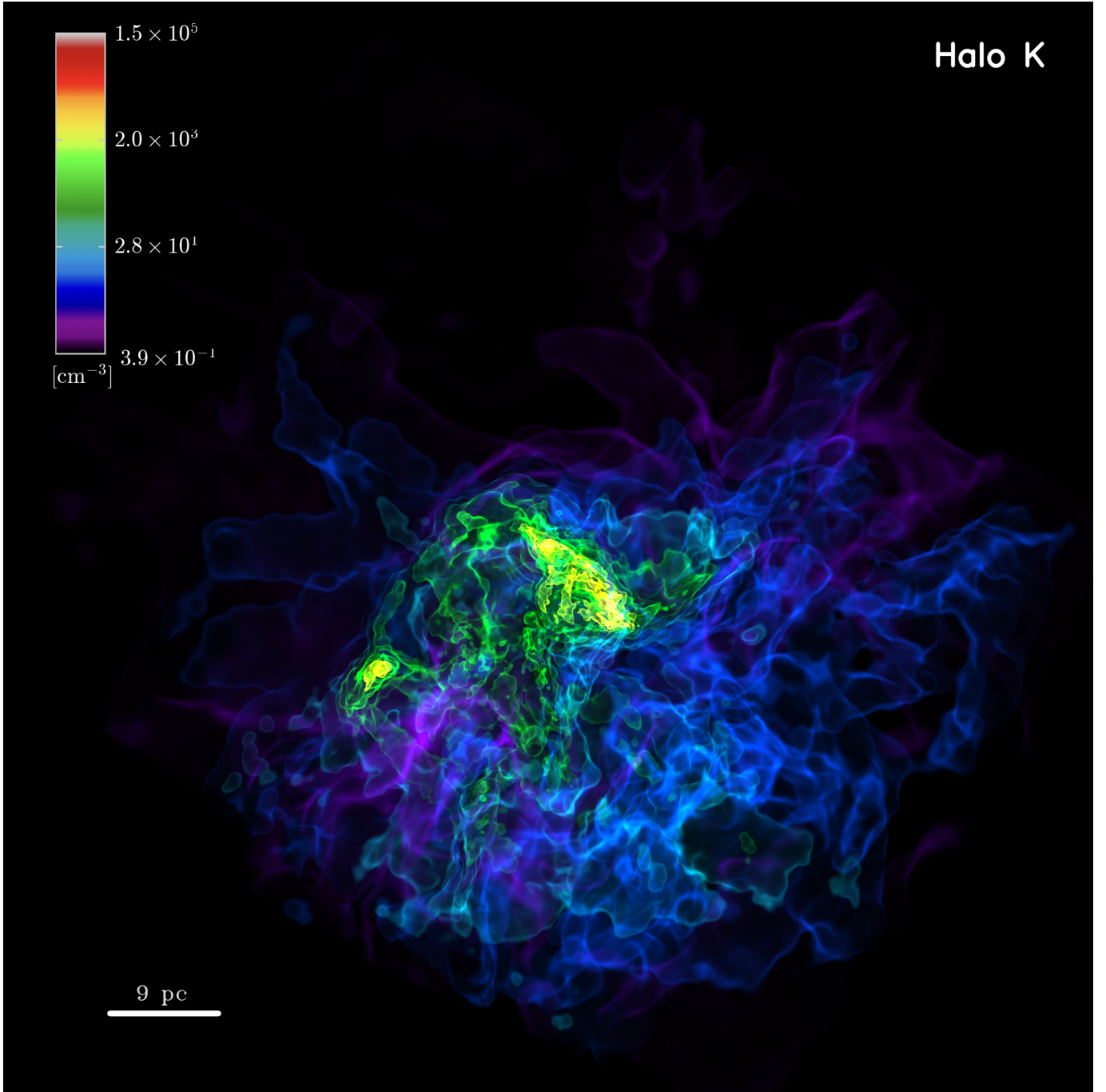


**Figure 10.** 3D gas density structure within  $0.1 R_{\text{vir}}$  of **Halo K**, highlighting two distinct clumps (visible as separate yellow-green nuggets). The detailed substructures within these clumps illustrate the influence of supersonic turbulence in the first star-forming region. Both clumps are expected to grow further through continued gas accretion and eventually collapse to form stars. The final mass of each clump sets an upper limit on the mass of the stars that may form within them.

& Chen (2024). In some halos, a small fraction of gas ( $\sim 0.01$ – $0.1\%$ ) can even reach  $\mathcal{M} > 10$ . We also find a positive correlation between the characteristic  $\mathcal{M}$  and the minihalo mass.

Each minihalo contains approximately  $10^2$ – $10^3 M_{\odot}$  of dense gas ( $n \geq 10^5 \text{ cm}^{-3}$ ) that is expected to collapse and form Pop III stars. This range of potential stellar mass is broadly consistent with previous studies (Abel et al. 1998; Bromm 2013). However, the supersonic turbulence in our simulations disrupts the spherical symmetry of the gas clouds, leading to the formation of clumpy structures, as shown in Figure 9. In several halos, such as **H** and **D**, multiple dense clumps are identified. These clumpy clouds

give rise to multiple dense cores, each potentially forming a star. The masses of these clumps range from  $2.6 M_{\odot}$  to  $66.5 M_{\odot}$ , setting an upper bound on the mass of Pop III stars in the absence of further clump mergers. The emergence of such clumps lowers the mass scale of individual Pop III stars and represents a fundamental shift from the disk fragmentation scenario observed in prior studies at AU scales (Turk et al. 2009; Clark et al. 2011; Greif 2015; Chiaki & Yoshida 2022).

## 5. CONCLUSION

We investigate the universality and diversity of supersonic turbulence in primordial halos by simulating the formation of 15 minihalos. Our GIZMO simulations use initial conditions drawn from large-scale cosmological IllustrisTNG simulations, enhanced by a robust particle-splitting technique to assess the turbulent structures within primordial gas clouds—the birthplaces of Pop III stars. The results show that the turbulence arises naturally from gas accretion into the gravitational potential wells of dark matter during minihalo formation. Gas velocities in the minihalos span from subsonic to supersonic, reaching  $\mathcal{M}$  up to  $\sim 30$ , clearly indicating the presence of supersonic turbulence.

In the central regions of halos, turbulent gas exhibits significant compressibility and vorticity, coinciding with high-density zones where molecular hydrogen cooling becomes efficient. The characteristic  $\mathcal{M}$  of halos lies between 2 and 5 and correlates positively with halo mass. Supersonic turbulence disrupts spherical collapse, producing clumpy filamentary structures, consistent with predictions by Tang & Chen (2024). The physical properties of primordial turbulence revealed by our simulations offer critical insights into the long-standing problem of Pop III star formation. Our findings help to constrain the mass scale of the first stars that soon will be examined high- $z$  observations with the James Webb Space Telescope (JWST).

Authors thank Chi-Hung Lin, Po-Feng Wu, and Chong-Yuan Hwang for their useful discussions. We also thank Ching-Yao Tang for his help with the data analysis. KC acknowledges the support of the Alexander von Humboldt Foundation and Heidelberg Institute for Theoretical Studies. This research is supported by the National Science and Technology Council, Taiwan, under grant No. MOST 110-2112-M-001-068-MY3, NSTC 113-2112-M-001-028-, and the Academia Sinica, Taiwan, under a career development award under grant No. AS-CDA-111-M04. This research was supported in part by grant NSF PHY-2309135 to the Kavli Institute for Theoretical Physics (KITP) and grant NSF PHY-2210452 to the Aspen Center for Physics. Our computing resources were supported by the National Energy Research Scientific Computing Center (NERSC), a U.S. Department of Energy Office of Science User Facility operated under Contract No. DE-AC02-05CH11231 and the TIARA Cluster at the Academia Sinica Institute of Astronomy and Astrophysics (ASIAA).

## REFERENCES

- Abel, T., Bryan, G. L., & Norman, M. L. 1998, The Formation and Fragmentation of Primordial Molecular Clouds, [arXiv:astro-ph/9810215 \[astro-ph\]](#)
- . 2002, *Science*, **295**, 93–98
- Bagla, J. S. 2002, *Journal of Astrophysics and Astronomy*, **23**, 185
- Bode, P., & Ostriker, J. P. 2003, *ApJS*, **145**, 1
- Bromm, V. 2013, *Reports on Progress in Physics*, **76**, 112901
- Bromm, V., Coppi, P. S., & Larson, R. B. 2002, *The Astrophysical Journal*, **564**, 23
- Chen, K.-J., Bromm, V., Heger, A., Jeon, M., & Woosley, S. 2015, *ApJ*, **802**, 13
- Chen, K.-J., Ho, M.-Y., & Tung, P.-C. 2025, Formation of Supersonic Turbulence in the Primordial Star-forming Cloud, [arXiv:2505.18964 \[astro-ph.GA\]](#)
- Chen, K.-J., Tang, C.-Y., Whalen, D. J., et al. 2024, *ApJ*, **964**, 91
- Chiaki, G., & Yoshida, N. 2022, *MNRAS*, **510**, 5199
- Clark, P. C., Glover, S. C. O., Smith, R. J., et al. 2011, *Science*, **331**, 1040
- Glover, S. C. O., & Abel, T. 2008, *Monthly Notices of the Royal Astronomical Society*, **388**, 1627–1651
- Gnedin, N. Y., Semenov, V. A., & Kravtsov, A. V. 2018, *Journal of Computational Physics*, **359**, 93
- Greif, T. H. 2015, *Computational Astrophysics and Cosmology*, **2**
- Grudić, M. Y., Guszejnov, D., Offner, S. S. R., et al. 2022, *MNRAS*, **512**, 216
- He, C.-C., & Ricotti, M. 2023, *MNRAS*, **522**, 5374
- Hirano, S., Hosokawa, T., Yoshida, N., et al. 2014, *The Astrophysical Journal*, **781**, 60
- Hirano, S., Hosokawa, T., Yoshida, N., et al. 2014, *ApJ*, **781**, 60
- Hopkins, P. F. 2015, *Monthly Notices of the Royal Astronomical Society*, **450**, 53–110
- Hosokawa, T., Hirano, S., Kuiper, R., et al. 2016, *The Astrophysical Journal*, **824**, 119
- Ishigaki, M. N., Tominaga, N., Kobayashi, C., & Nomoto, K. 2018, *The Astrophysical Journal*, **857**, 46
- Ji, A. P., Curtis, S., Storm, N., et al. 2024, *ApJL*, **961**, L41
- Klessen, R. S., & Glover, S. C. O. 2023, The first stars: formation, properties, and impact, [arXiv:2303.12500 \[astro-ph.CO\]](#)
- Kolmogorov, A. N. 1991, *Proceedings: Mathematical and Physical Sciences*, **434**, 9

- Marinacci, F., Vogelsberger, M., Pakmor, R., et al. 2018, *MNRAS*, **480**, 5113
- Mathew, S. S., & Federrath, C. 2021, *Monthly Notices of the Royal Astronomical Society*, **507**, 2448
- Menon, S. H., Federrath, C., Klaassen, P., Kuiper, R., & Reiter, M. 2020a, *Monthly Notices of the Royal Astronomical Society*, **500**, 1721
- Menon, S. H., Federrath, C., & Kuiper, R. 2020b, *Monthly Notices of the Royal Astronomical Society*, **493**, 4643
- Naiman, J. P., Pillepich, A., Springel, V., et al. 2018, *MNRAS*, **477**, 1206
- Nelson, D., Pillepich, A., Springel, V., et al. 2018, *MNRAS*, **475**, 624
- Norman, M. L. 2008, *AIP Conference Proceedings*, **990**, 3
- Omukai, K. 2001, *ApJ*, **546**, 635
- Omukai, K., & Palla, F. 2001, *ApJL*, **561**, L55
- Omukai, K., & Palla, F. 2003, *The Astrophysical Journal*, **589**, 677
- O’Shea, B. W., & Norman, M. L. 2007, *ApJ*, **654**, 66
- Pillepich, A., Nelson, D., Hernquist, L., et al. 2018, *MNRAS*, **475**, 648
- Ramesh, R., & Nelson, D. 2024, *MNRAS*, **528**, 3320
- Ramesh, R., Nelson, D., Fielding, D., & Brüggén, M. 2024, *A&A*, **684**, L16
- Sharda, P., & Menon, S. H. 2024, *arXiv e-prints*, arXiv:2405.18265
- Shukurov, A. 2011, Introduction to Interstellar Turbulence
- Skúladóttir, Á., Vanni, I., Salvadori, S., & Lucchesi, R. 2024, *A&A*, **681**, A44
- Smith, B. D., Turk, M. J., Sigurdsson, S., O’Shea, B. W., & Norman, M. L. 2009, *The Astrophysical Journal*, **691**, 441
- Smith, B. D., Bryan, G. L., Glover, S. C. O., et al. 2017, *MNRAS*, **466**, 2217
- Springel, V. 2005, *MNRAS*, **364**, 1105
- . 2010, *MNRAS*, **401**, 791
- Springel, V., White, S. D. M., Tormen, G., & Kauffmann, G. 2001, *MNRAS*, **328**, 726
- Springel, V., Pakmor, R., Pillepich, A., et al. 2018, *MNRAS*, **475**, 676
- Stacy, A., Greif, T. H., & Bromm, V. 2010, *MNRAS*, **403**, 45
- Stiavelli, M. 2009, From First Light to Reionization: The End of the Dark Ages (WILEY)
- Tang, C.-Y., & Chen, K.-J. 2024, Clumpy Structures within the Turbulent Primordial Cloud, *arXiv:2303.00751 [astro-ph.GA]*
- Tegmark, M., Silk, J., Rees, M. J., et al. 1997, *The Astrophysical Journal*, **474**, 1–12
- Truelove, J. K., Klein, R. I., McKee, C. F., et al. 1998, *The Astrophysical Journal*, **495**, 821
- Tung, P.-C., & Chen, K.-J. 2024, *arXiv e-prints*, arXiv:2412.16440
- Turk, M. J., Abel, T., & O’Shea, B. 2009, *Science*, **325**, 601
- Turk, M. J., Smith, B. D., Oishi, J. S., et al. 2011, *The Astrophysical Journal Supplement Series*, **192**, 9
- Umeda, H., & Nomoto, K. 2005, *The Astrophysical Journal*, **619**, 427
- Weinberger, R., Springel, V., Hernquist, L., et al. 2016, *Monthly Notices of the Royal Astronomical Society*, **465**, 3291–3308
- Xu, G. 1995, *ApJS*, **98**, 355
- Yoshida, N., Abel, T., Hernquist, L., & Sugiyama, N. 2003, *The Astrophysical Journal*, **592**, 645–663
- Yuen, K. H., Ho, K. W., Law, C. Y., Chen, A., & Lazarian, A. 2022, Turbulent universal galactic Kolmogorov velocity cascade over 6 decades, *arXiv:2204.13760 [astro-ph.GA]*